



Effect of transition metal doping on the catalytic performance of Au–Pd/3DOM Mn₂O₃ for the oxidation of methane and o-xylene



Shaohua Xie^a, Yuxi Liu^{a,*}, Jiguang Deng^{a,*}, Xingtian Zhao^a, Jun Yang^a, Kunfeng Zhang^a, Zhuo Han^a, Hamidreza Arandiyani^b, Hongxing Dai^{a,*}

^a Beijing Key Laboratory for Green Catalysis and Separation, Key Laboratory of Beijing on Regional Air Pollution Control, Key Laboratory of Advanced Functional Materials, Education Ministry of China, and Laboratory of Catalysis Chemistry and Nanoscience, Department of Chemistry and Chemical Engineering, College of Environmental and Energy Engineering, Beijing University of Technology, Beijing 100124, China

^b Particles and Catalysis Research Group, School of Chemical Engineering, The University of New South Wales, Sydney, NSW 2052, Australia

ARTICLE INFO

Article history:

Received 20 September 2016

Received in revised form

15 December 2016

Accepted 12 January 2017

Available online 13 January 2017

Keywords:

Transition metal-doped Au–Pd nanoparticle
Three-dimensionally ordered macroporous
Mn₂O₃
Methane oxidation
O-xylene oxidation
Oxygen activation

ABSTRACT

Palladium-based catalysts are highly active for eliminating volatile organic compounds. Reducing the use of noble metals and enhancing performance of a catalyst are always desirable. The three-dimensionally ordered macroporous (3DOM) Mn₂O₃-supported transition metal *M* (*M*=Mn, Cr, Fe, and Co)-doped Au–Pd nanoparticles (NPs) with an Au–Pd–x*M* loading of 1.86–1.97 wt% were prepared using the modified polyvinyl alcohol-protected reduction method. It is found that the Au–Pd–x*M* NPs with a size of 3.6–4.4 nm were highly dispersed on the surface of 3DOM Mn₂O₃. The 1.94 wt% Au–Pd–0.21Co/3DOM Mn₂O₃ and 1.94 wt% Au–Pd–0.22Fe/3DOM Mn₂O₃ samples performed the best for the oxidation of methane and o-xylene, respectively. The methane oxidation rate at 340 °C (339.0 × 10^{−6} mol/(g_{Pd} s)) over 1.94 wt% Au–Pd–0.21Co/3DOM Mn₂O₃ was three times higher than that (93.8 × 10^{−6} mol/(g_{Pd} s)) over 1.97 wt% Au–Pd/3DOM Mn₂O₃, and the o-xylene reaction rate at 140 °C (2.59 μmol/(g_N s)) over 1.94 wt% Au–Pd–0.22Fe/3DOM Mn₂O₃ was two times higher than that (0.93 μmol/(g_N s)) over 1.97 wt% Au–Pd/3DOM Mn₂O₃. It is concluded that doping a certain amount of the transition metal to Au–Pd/3DOM Mn₂O₃ could modify the microstructure of the alloy NPs, thus improving the oxygen activation and methane adsorption ability. We are sure that the *M*-doped Au–Pd/3DOM Mn₂O₃ materials are promising catalysts for the efficient removal of volatile organic compounds.

© 2017 Elsevier B.V. All rights reserved.

1. Introduction

Most of volatile organic compounds (VOCs) are harmful to the atmosphere and human health. Catalytic oxidation has been regarded as one of the most promising approaches for abatement of VOCs owing to its high efficiency and low operation temperatures [1–3]. Supported noble metal catalysts perform well for the oxidation of VOCs at low temperatures as compared with transition-metal oxide catalysts [3–7]. For instance, the reaction temperature (ca. 200 °C) at an o-xylene conversion of 100% over Pd/Co₃O₄ (3D) was much lower than that (ca. 300 °C) over Co₃O₄ (3D) [4]. Au/γ-MnO₂ exhibited much better catalytic activity than γ-MnO₂ for the oxidation of toluene, acetaldehyde, and hexane [5]. However, reducing the cost of a

catalyst and enhancing its catalytic activity and (hydro)thermal stability are always demanded in practical applications.

A number of works have demonstrated that alloying Pd with Au could give rise to a catalyst which showed high activity and stability in the redox-involving reactions [8–14]. For example, Hutchings et al. synthesized a series of the supported Au–Pd catalysts, and found that these materials showed excellent catalytic activity and selectivity for the direct synthesis of H₂O₂ [8] and the oxidation of alcohols [9], toluene [10], and methane [11]. In the previous works, we have shown that porous transition-metal oxide-supported Au–Pd nanoparticles (NPs) exhibit high catalytic activity and (hydro)thermal stability for the combustion of toluene and methane [12–14]. However, the high cost of these noble metal-based materials still limits their practical applications. It has recently been reported that doping a certain amount of a base metal to the noble metal NPs was a facile way to reduce the amount of the noble metal used in the catalyst, and the base metal-doped catalyst performed well and showed good stability for some reactions [15–20]. For instance, introducing a certain amount of Sn to

* Corresponding authors.

E-mail addresses: yxliu@bjut.edu.cn (Y. Liu), jgdeng@bjut.edu.cn (J. Deng), hxdai@bjut.edu.cn (H. Dai).

Pd (instead of Au) gave rise to more than 95% H₂O₂ selectivity in the direct synthesis of H₂O₂ [15]. With the doping of Sn or Fe to the Pt NPs, the selectivity was enhanced in the hydrogenation of unsaturated aldehydes [16]. Working on the oxidation of ethanol over the supported noble metal catalysts, Dutta and Ouyang observed a synergistic effect of Au–Pt–Ni on the improved catalytic performance [17]. It is generally believed that the amount of active sites can be increased in the supported noble metal catalyst by introducing the base metal to the noble metal NPs [16–18]. We envision that generating the supported Au–Pd–M ($M = \text{Cr, Mn, Fe, and Co}$) NPs would meet the requirements for achieving high catalytic performance and good stability as well as effective utilization of noble metals in the oxidation of organics.

Due to the low cost and environmentally friendly feature, Mn₂O₃ has been extensively used as catalyst or support for the removal of VOCs [2,21,22]. Compared with the bulk counterpart, the porous Mn₂O₃ with a rich porosity, a high surface area, and a good reducibility is expected to possess improved physicochemical properties [23]. Because of the unique characteristics of easy mass transfer and diffusion, the catalysts with a three-dimensionally ordered macroporous (3DOM) structure have recently been demonstrated to perform excellently for the combustion of soot and VOCs [23–26]. Previously, our group adopted the polymethyl methacrylate (PMMA)-templating and polyvinyl alcohol (PVA)-protected reduction strategies to successfully generate a series of 3DOM-structured materials [3,23], and found that most of them showed good catalytic activity for VOCs oxidation. Herein, we report for the first time the fabrication of 3DOM Mn₂O₃-supported Au–Pd–xM NPs (Au–Pd–xM/3DOM Mn₂O₃: x was the M/Pd mass ratio, $M = \text{Mn, Cr, Fe, and Co}$) using the PMMA-templating and modified PVA-protected reduction strategies. It is found that the M-doped Au–Pd/3DOM Mn₂O₃ materials performed well for the oxidative removal of methane and o-xylene. We are sure that the strategy of doping a transition metal into Au–Pd NPs may provide a valuable reference on the design of catalysts for the total oxidation of VOCs.

2. Experimental

2.1. Catalyst preparation

The PMMA microspheres were synthesized according to the procedure described elsewhere [27], and the average size of PMMA spheres were ca. 300 nm. 3DOM Mn₂O₃ was fabricated according to the procedures described elsewhere [22]. In a typical fabrication, 20 mmol of 50 wt% Mn(NO₃)₂ aqueous solution was added to 8.0 mL of ethylene glycol (EG) and methanol (MeOH) solution (EG/MeOH volumetric ratio = 1:3) at room temperature (RT) under stirring for 1 h, obtaining a transparent solution. Then, 2.0 g of the PMMA template was soaked in the above transparent solution for 6 h. After being filtered and dried at RT for 48 h, the obtained powders were calcined in a N₂ flow of 200 mL/min at a ramp of 1 °C/min from RT to 300 °C and kept at 300 °C for 2 h, then cooled to 50 °C in the same atmosphere, and finally heated in an air flow of 200 mL/min at a ramp of 1 °C/min from RT to 500 °C and maintained at this temperature for 10 h, thus generating the 3DOM Mn₂O₃ support.

The Au–Pd–xM (x was the M/Pd mass ratio; $M = \text{Mn, Cr, Fe, and Co}$) NPs were prepared via a modified PVA-protected reduction route with PVA (MW = 10,000 g/mol) as protecting agent and NaBH₄ as reducing agent. The typical preparation procedure is as follows: A desired amount of PVA (noble metal/PVA mass ratio = 1.00:1.50) was added to a mixed aqueous solution of HAuCl₄ and PdCl₂ (Au/Pd molar ratio = 0.54:1.00) in an ice bath under vigorous stirring for 15 min, and then a desired amount of the M-containing (MnCl₂, CrCl₃, FeCl₂ or CoCl₂) aqueous solution (1.50 mmol/L; the

theoretical $x = 0, 0.10, 0.20, 0.50$, and 2.00), and a HCl aqueous solution (3.00 mol/L; Pd/HCl molar ratio = 1.00:5.00) were added to the above noble metal-containing mixed solution. After vigorous stirring for 30 min, a NaBH₄ aqueous solution (2.00 g/L; metal/NaBH₄ molar ratio = 1.00:5.00) was rapidly injected to form a dark brown suspension, thus obtaining the suspension of Au–Pd–xM NPs after further stirring for 1 h.

The 3DOM Mn₂O₃-supported Au–Pd–xM samples were prepared using the gas bubble-assisted adsorption strategy. A desired amount of the 3DOM Mn₂O₃ support was added to the obtained Au–Pd–xM suspension with a theoretical Au–Pd–M loading of 2.00 wt%. Such a suspension was subjected to ultrasonic (60 kHz) treatment for 10 min. The gas bubble-assisted adsorption operation with a three-necked bottle was used to make the reaction homogenous. After bubbling the suspension with N₂ (100 mL/min) for 4 h, the wet solid was filtered, washed with deionized water (until no Cl[−] ions were detected in the filtrate), dried at 80 °C for 12 h, and calcined in a N₂ flow of 100 mL/min at a ramp of 10 °C/min from RT to 500 °C and kept at 500 °C for 1 h, thus obtaining the Au–Pd–xM/3DOM Mn₂O₃ samples. The results of inductively coupled plasma atomic emission spectroscopic (ICP–AES) investigations reveal that the real Au–Pd–xM loadings (1.86–1.97 wt%) were rather similar in each of the samples. All of the chemicals (A.R. in purity) are purchased from Beijing Chemical Reagents Company and used without further purification.

2.2. Catalyst characterization

All of the samples were characterized by means of techniques, such as ICP–AES, X-ray diffraction (XRD), scanning electron microscopy (SEM), transmission electron microscopy (TEM), high angle annular dark field (HAADF) and elemental mapping, X-ray photoelectron spectroscopy (XPS), hydrogen temperature-programmed reduction (H₂-TPR), and oxygen temperature-programmed desorption (O₂-TPD). The detailed characterization procedures are described in the Supplementary material.

2.3. Catalytic activity evaluation

Catalytic activities of the samples were evaluated in a continuous flow fixed-bed quartz tubular microreactor (i.d. = 6.0 mm). As illustrated in scheme S1, the thermocouple was inserted to a small quartz tube in the quartz tubular microreactor, in which the bottom directly contacted the catalyst bed, thus detecting the reaction temperatures during the VOC oxidation processes. To minimize the effect of hot spots, 50 mg of the sample (40–60 mesh) was diluted with 0.25 g of quartz sands (40–60 mesh). During the experiments, the gas inlet flow rate was varied from 16.6 to 166.0 mL/min, thus giving a space velocity (SV) of 20,000–200,000 mL/(g h) or a gas hourly space velocity (GHSV) of 19,100–191,000 h^{−1}. Before the test, each sample was pretreated in an oxygen flow of 30 mL/min at 300 °C for 1 h. For methane oxidation, the reactant mixture was composed of 2.5 vol% CH₄ + 20.0 vol% O₂ + 77.5 vol% N₂ (balance), the concentration of methane was slightly higher than that (1.0–2.0 vol%) reported in literature. At the methane concentration of 2.5 vol%, we observed the effect of doped transition metal on catalytic performance of the Au–Pd samples; for o-xylene oxidation, the reactant mixture was 1000 ppm o-xylene + 20.0 vol% O₂ + N₂ (balance). The 1000-ppm o-xylene was generated by passing a N₂ flow through a pure o-xylene-containing bottle that was chilled in an isothermal bath at 0 °C. In the case of water vapor introduction, 5.0 vol% H₂O was introduced by passing the feed stream through a water saturator at 34 °C. Reactants and products were analyzed online by gas chromatography (GC-14C, Shimadzu) equipped with a flame ionization detector (FID) and a thermal conductivity detector (TCD), using

a stabilwax@-DA column (30 m in length) and a Carboxen 1000 column (3 m in length). The balance of carbon throughout the catalytic system was estimated to be $99.5 \pm 1.5\%$. Catalytic activities of the samples were evaluated using the temperatures ($T_{10\%}$, $T_{50\%}$, and $T_{90\%}$) required for achieving methane or *o*-xylene conversions of 10, 50, and 90%, respectively. Conversion was defined as $(c_{\text{inlet}} - c_{\text{outlet}})/c_{\text{inlet}} \times 100\%$, where the c_{inlet} and c_{outlet} were the inlet and outlet CH_4 or *o*-xylene concentrations in the feed stream, respectively.

The absence of mass-transfer limitations under reaction conditions was verified both experimentally and theoretically. The estimation of the Damköhler number under the most unfavorable conditions reveals that the external diffusion mass-transfer resistance was negligible. Making a Weisz–Prater analysis is a facile way to evaluate the presence of internal mass transfer limitation. According to the Weisz–Prater criterion, the dimensionless Weisz–Prater parameter (N_{W-P}) value is less than 0.3, which can be considered a sufficient condition for the absence of significant pore diffusion limitation [28]. For methane oxidation at 340°C over the Au–Pd–0.21Co/3DOM Mn_2O_3 sample, the N_{W-P} value was calculated to be 0.0758; for *o*-xylene oxidation at 170°C over the Au–Pd–0.22Fe/3DOM Mn_2O_3 sample, the N_{W-P} value was calculated to be 0.00334, the N_{W-P} values were much less than 0.3. Thermal effects were also negligible at a N_{W-P} value of less than 0.01 [29]. Therefore, we deduce that there was no significant heat or mass transfer limitation under the present reaction conditions. These assumptions were confirmed experimentally since the same conversion was obtained at different total flow rates. Furthermore, the axial dispersion effect can be neglected for a reactor diameter/particle diameter ratio higher than 10 and a catalytic bed length/particle diameter ratio higher than 50 [29]. In the present work, the values of the two ratios were 21 and 65, respectively. For the sake of clear presentation, the nomenclature and abbreviations of the variables and terms used in the present work are summarized in Table S1 of the Supplementary material.

3. Results

3.1. Metal loading, crystal phase composition, pore structure, and surface area

According to the results (Table 1) of the ICP-AES studies, the Au–Pd loading in Au–Pd/3DOM Mn_2O_3 was 1.97 wt%; the Au–Pd–*x*Mn (*x*=0.13, 0.21, 0.47, and 1.96) loadings in Au–Pd–*x*Mn/3DOM Mn_2O_3 were 1.96, 1.96, 1.96, and 1.86 wt%, respectively; and the Au–Pd–0.19Cr, Au–Pd–0.22Fe, and Au–Pd–0.21Co loadings in Au–Pd–0.19Cr/3DOM Mn_2O_3 , Au–Pd–0.22Fe/3DOM Mn_2O_3 , and Au–Pd–0.21Co/3DOM Mn_2O_3 were 1.95, 1.94, and 1.94 wt%, respectively.

The crystal phases of the 3DOM Mn_2O_3 -supported Au–Pd–*x*M samples were determined by the XRD technique. According to the standard Mn_2O_3 sample (JCPDS PDF# 41-1442), the XRD pattern of 3DOM Mn_2O_3 in the 3DOM Mn_2O_3 -supported Au–Pd–*M* samples could be indexed to a cubic crystal structure (Fig. S1). No apparent diffraction peaks assignable to the Au, Pd and/or *M* phases were recorded due to their low loadings and good dispersion, suggesting that the loading of Au–Pd–*x*M NPs did not result in an obvious change in crystal structure of Mn_2O_3 . Scherrer equation ($D = 0.89\lambda/(\beta\cos(\theta))$, where λ is the X-ray wavelength, β is the full width at half maximum (FWHM) of the (222) plane of Mn_2O_3 , and θ is the corresponding diffraction angle) was applied to calculate the grain sizes of Mn_2O_3 in the 3DOM Mn_2O_3 -supported Au–Pd–*x*M samples. As summarized in Table 1, the calculated grain sizes (46.7–48.6 nm) of Mn_2O_3 crystallites in the Au–Pd–*x*M/3DOM Mn_2O_3 samples were much similar.

Table 1
Average Mn_2O_3 crystallite sizes (D), real metal contents, pore volumes, BET surface areas, macropore diameters, and average metal particle sizes of the as-prepared samples.

Sample	XRD result	Real metal content ^b (wt%)			BET result	Pore volume (cm ³ /g)	Surface area (m ² /g)	Macropore diameter ^c (nm)	Average metal particle size (nm)
		Crystal phase	D^a (nm)	Au	Pd				
Au–Pd/3DOM Mn_2O_3	Cubic	48.2	0.99	0.98	—	1.97	0.189	377	180–195
Au–Pd–0.13Mn/3DOM Mn_2O_3	Cubic	48.4	0.91	0.93	0.12	1.96	0.183	38.5	180–200
Au–Pd–0.21Mn/3DOM Mn_2O_3	Cubic	46.7	0.88	0.89	0.19	1.96	0.185	38.1	185–200
Au–Pd–0.47Mn/3DOM Mn_2O_3	Cubic	47.5	0.81	0.78	0.37	1.96	0.169	37.4	175–195
Au–Pd–1.96Mn/3DOM Mn_2O_3	Cubic	47.3	0.47	0.47	0.92	1.86	0.174	38.2	180–205
Au–Pd–0.19Cr/3DOM Mn_2O_3	Cubic	48.1	0.89	0.89	0.17	1.95	0.167	36.9	185–205
Au–Pd–0.22Fe/3DOM Mn_2O_3	Cubic	48.6	0.87	0.88	0.19	1.94	0.188	37.4	175–200
Au–Pd–0.21Co/3DOM Mn_2O_3	Cubic	47.7	0.89	0.87	0.18	1.94	0.190	38.1	175–205

^a Data were calculated according to the Scherrer equation using the FWHM of the (222) line of Mn_2O_3 .

^b Data were determined by the ICP-AES technique.

^c Data were estimated according to the SEM images.

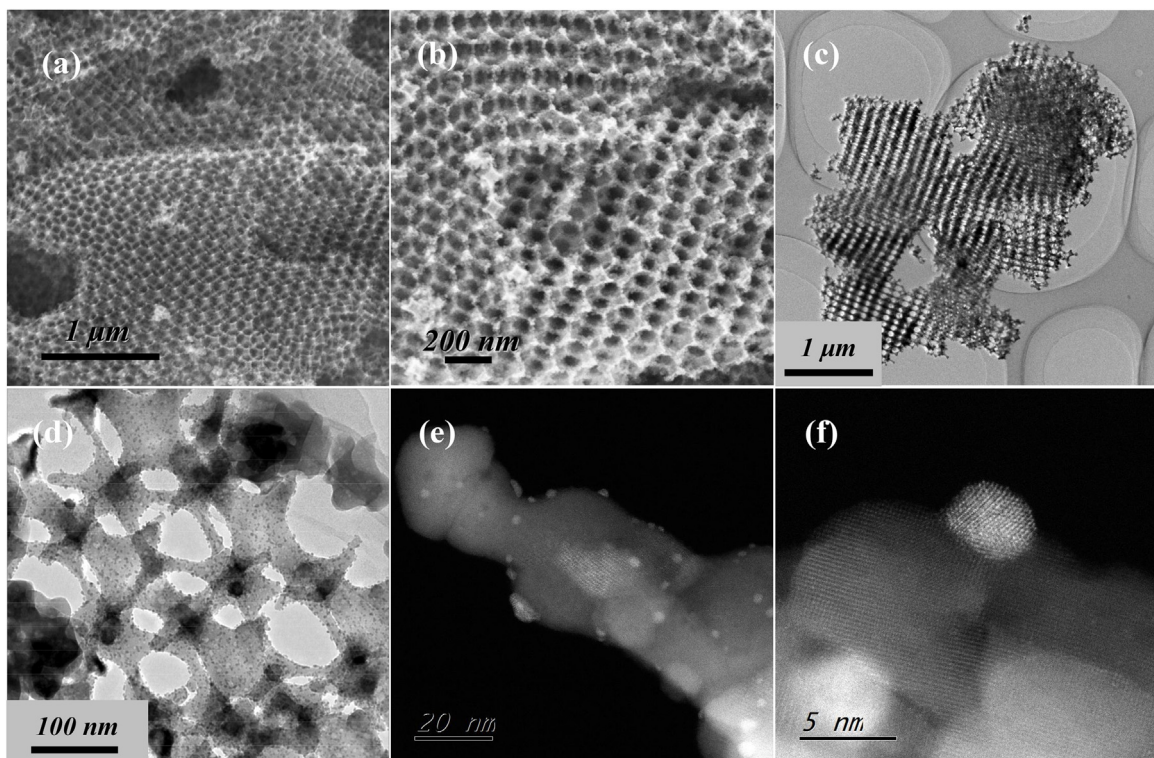


Fig. 1. (a,b) SEM, (c,d) TEM, and (e,f) HAADF-STEM images of the Au–Pd–0.47Mn/3DOM Mn₂O₃ sample.

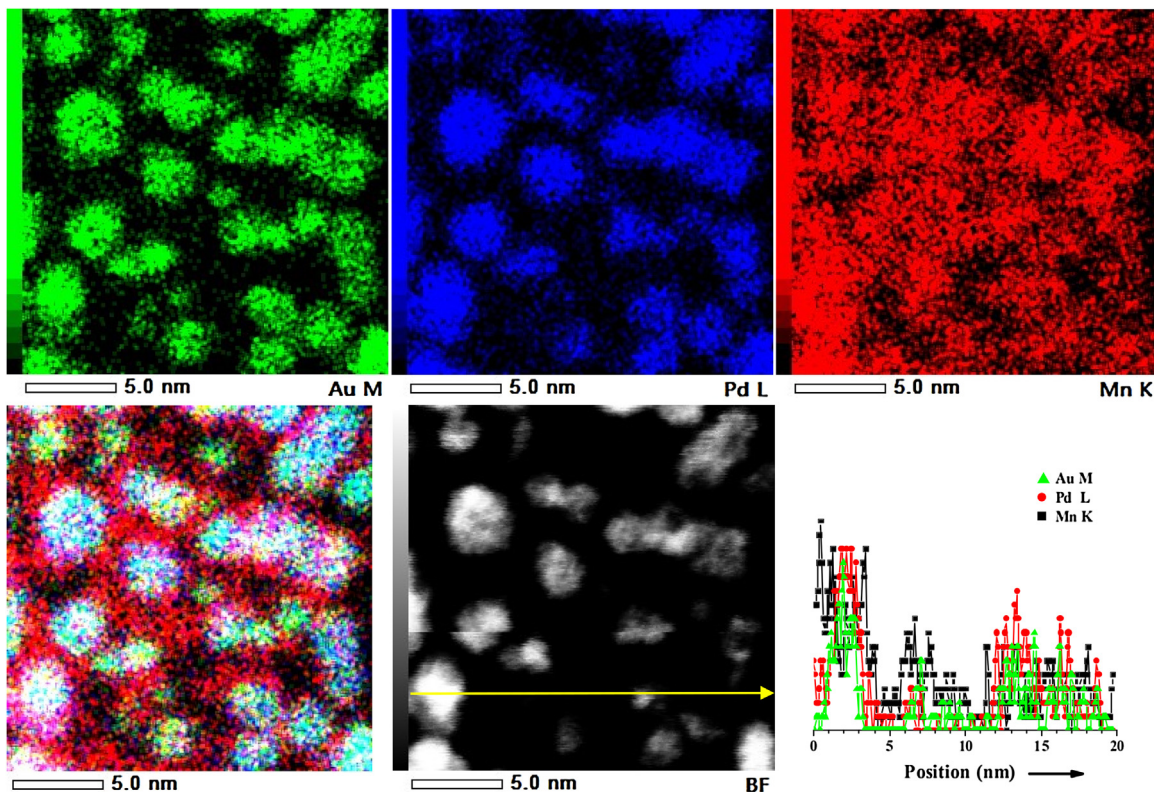


Fig. 2. Elemental analysis images of the Au–Pd–0.47 Mn NPs.

Fig. 1 shows the SEM, TEM, and HAADF-STEM images of the typical sample, similar to our previous results [12]. High-quality 3DOM architectures with a pore-size range of 175–205 nm were observed in the Au–Pd–0.47Mn/3DOM Mn₂O₃ sample. A number

of Au–Pd–0.47 Mn NPs were highly dispersed on the surface of 3DOM Mn₂O₃. By estimating the particle sizes of 200 NPs on TEM images, one can realize that the mean diameter of the Au–Pd–M NPs was in the range of 3.6–4.4 nm (Table 1 and Fig. S2). The sizes

of Au–Pd– x Mn NPs in the samples were in the range of 3.8–4.4 nm. With the rise in Mn content, the Au–Pd– x Mn particles grew slightly, and the Au–Pd–1.96 Mn NPs possessed the biggest size of 4.4 nm. In order to confirm the structure of the as-prepared NPs, an elemental analysis on the Au–Pd–0.47 Mn NPs was made. It can be observed from Fig. 2 that the mono-dispersed NPs were composed of Au, Pd, and Mn, in which the three elements were well distributed. The results of line element scan analysis again demonstrate the presence of a well-mixed cluster of Au–Pd–0.47 Mn NPs. In other words, using the modified PVA-protected reduction method could facilely generate uniform ternary metal clusters (e.g., Au–Pd–M).

Fig. 3A shows the N_2 adsorption–desorption isotherms of the 3DOM Mn_2O_3 -supported Au–Pd– x M samples. These samples exhibited a type II isotherm with a H3 hysteresis loop in the relative pressure (p/p_0) range of 0.8–1.0. There was also a slight H2 type hysteresis loop in the p/p_0 range of 0.2–0.8. The H3 hysteresis loop, which did not clearly show any adsorption plateau at p/p_0 close to unity, was related to the existence of slit-shaped pores in the materials, which is indicative of macropore formation [24]. The low-pressure portion of the almost linear middle section of the isotherm, which can be attributed to unrestricted mono- or multi-layer adsorption, also suggests formation of macropores [25]. These results were in good agreement with those of the SEM and TEM (Fig. 1) investigations and pore-size distributions (Fig. 3B) of the samples. Each of the samples displayed a broad pore-size distribution scattered from 10 to 150 nm. Surface areas and pore volumes of the samples are summarized in Table 1. It is observed that these supported Au–Pd–M samples showed a similar surface area and a similar pore volume of 36.9–38.5 m^2/g and 0.169–0.190 cm^3/g , respectively.

3.2. Catalytic performance, effect of water vapor, and apparent activation energy

Methane is a greenhouse gas that its global warming potential is dozens of times higher than that of CO_2 . Fig. 4 shows the methane conversion as a function of reaction temperature over the as-prepared samples. It should be noted that the catalytic performance evaluation of all of the samples at different temperatures was carried out at least 4 times, the conversion data were the average values obtained in the several tests. For example, the obtained methane conversions were almost the same in the first and second runs (Fig. S3). That is to say, all of the activity data were reliable. Preliminarily, we prepared the Au–Pd– x Mn/3DOM Mn_2O_3 ($x=0.13, 0.21, 0.47$, and 1.96) samples to examine the effect of Mn/Pd mass ratio on methane oxidation. It is observed that the doping of Mn caused a slight decrease in catalytic activity. Among the Mn-doped samples, however, the sample with a Mn/Pd mass ratio of 0.21 performed the best (Table S2 and Fig. 4A). Therefore, we synthesized the 3DOM Mn_2O_3 -supported Au–Pd– x M ($x=ca. 0.20$; $M=Mn, Cr, Fe$, and Co) samples. Obviously, the catalytic activity was enhanced by doping Co or Cr to the supported Au–Pd NPs (Fig. 4B and Table S2). The catalytic activity decreased in the sequence of Au–Pd–0.21Co/3DOM Mn_2O_3 > Au–Pd–0.19Cr/3DOM Mn_2O_3 > Au–Pd/3DOM Mn_2O_3 > Au–Pd–0.22Fe/3DOM Mn_2O_3 . After methane conversions reached higher than 95%, they increased slowly to 100% with the rise in reaction temperature (Fig. 4). However, methane could be totally oxidized above 580 °C over all of these samples (not shown in Fig. 4). A possible reason accountable for the slow conversion increase at temperatures above 500 °C might be due to the crystal growth of the alloy NPs as well as Mn_2O_3 since the samples were prepared after calcination at 500 °C. The outlet gas was examined by MS (Hiden QGA), the CO_2 selectivity was above 99% according to the carbon balance. That is to say, there were no byproducts formed in methane oxidation above 300 °C over these supported

Au–Pd–M catalysts. Among all of the samples, Au–Pd–0.21Co/3DOM Mn_2O_3 performed the best, especially its low-temperature performance ($T_{10\%}=322$ °C and $T_{50\%}=365$ °C). As listed in Table S2, the $T_{90\%}$ (442 °C) over Au–Pd–0.21Co/3DOM Mn_2O_3 (2.5 vol% CH_4 at $SV=40,000$ mL/(g h)) was much lower than that (ca. 640 °C) over 0.5 wt% Pd/ZrO₂ (900) (1.0 vol% CH_4 at $SV=120,000$ mL/(g h)) [30], that (ca. 525 °C) over 1 wt% Pd/Gd_{0.1}Ce_{0.9}O_{1.95} (CC) (2.8 vol% CH_4 at $SV=66,667$ mL/(g h)) [31], that (ca. 520 °C) over 1.0 wt% Co–1.0 wt% Pd/Al₂O₃ (0.4 vol% CH_4 at $SV=300,000$ mL/(g h)) [32], that (ca. 480 °C) over 1.0 wt% Co_{3.5}Pd/3DOM CeO₂ (2.5 vol% CH_4 at $SV=40,000$ mL/(g h)) [33], similar to that (ca. 405 °C) over 1.0 wt% Pd@ZrO₂/Si–Al₂O₃ (1.0 vol% CH_4 at $SV=18,000$ mL/(g h)) [34], but higher than that (ca. 343 °C) over 1.97 wt% Au_{0.45}Pd/meso-Co₃O₄ (2.5 vol% CH_4 at $SV=20,000$ mL/(g h)) [14]. Therefore, our Au–Pd–0.21Co/3DOM Mn_2O_3 catalyst outperformed most of the above catalysts reported in the literature.

Since PdO is the active phase for methane oxidation over the Pd-based catalysts, methane oxidation rates at 340 °C can be calculated according to the activity data and amounts of Pd in the Au–Pd– x M/3DOM Mn_2O_3 samples, and the results are summarized in Table S2. Methane oxidation rate at 340 °C (339.0×10^{-6} mol/(g_{Pd} s)) over Au–Pd–0.21Co/3DOM Mn_2O_3 was three times higher than that (93.8×10^{-6} mol/(g_{Pd} s)) over Au–Pd/3DOM Mn_2O_3 , and nearly twice as much as that (172.2×10^{-6} mol/(g_{Pd} s)) over Co_{3.5}Pd/3DOM CeO₂ [33], significantly higher than that (136.1×10^{-6} mol/(g_{Pd} s)) over 1.0 wt% Co–1.0 wt% Pd/Al₂O₃ [32], that (232.8×10^{-6} mol/(g_{Pd} s)) over 0.5 wt% Pd/Ce–Zr–Cr/Al₂O₃ [35], and that (255.4×10^{-6} mol/(g_{Pd} s)) over 1 wt% Pd/Gd_{0.1}Ce_{0.9}O_{1.95} (CC) [31], but lower than that (466.5×10^{-6} mol/(g_{Pd} s)) over 1.97 wt% Au_{0.45}Pd/meso-Co₃O₄ [14]. These results indicate that doping Co to Au–Pd/3DOM Mn_2O_3 enhanced its catalytic performance for methane oxidation, implying that there were other factors (e.g., methane adsorption ability enhanced by the doped transition metals [33]) that could influence the catalytic performance for methane oxidation apart from the Pd species. The 3DOM Mn_2O_3 -supported Au–Pd–0.21Co sample was more active for methane oxidation than most of the catalysts reported in the literature. Considering that methane/oxygen volumetric ratio was 1/8 in methane oxidation, it is hard to determine the order of methane oxidation. Hence, we did not calculate the apparent activation energies of methane oxidation over the catalysts. As a typical VOC, *o*-xylene was selected for evaluating the catalytic activities of the Au–Pd– x M/3DOM Mn_2O_3 samples. It can be clearly observed from Fig. 5A that *o*-xylene conversion increased with the rise in temperature. Apart from Au–Pd–0.19Cr/3DOM Mn_2O_3 , the other transition-metal-doped Au–Pd/3DOM Mn_2O_3 samples performed better than the Au–Pd/3DOM Mn_2O_3 sample at a SV of 40,000 mL/(g h). The Au–Pd–0.22Fe/3DOM Mn_2O_3 sample showed the best activity ($T_{10\%}=140$ °C and $T_{90\%}=213$ °C) for *o*-xylene oxidation. The catalytic performance decreased in the sequence of Au–Pd–0.22Fe/3DOM Mn_2O_3 > Au–Pd–0.21Mn/3DOM Mn_2O_3 > Au–Pd–0.21Co/3DOM Mn_2O_3 > Au–Pd/3DOM Mn_2O_3 > Au–Pd–0.19Cr/3DOM Mn_2O_3 . Considering that the Au and/or Pd species are highly active for *o*-xylene oxidation at low temperatures, it is very hard to determine the real active sites in the Au–Pd– x M/3DOM Mn_2O_3 catalysts. That is, the accurate calculation of turnover frequencies (TOFs) over such catalysts is difficult. The TOF_N (TOF_N= X_0/n_N , where X is the conversion at a certain temperature, X_0 (mol/s) is the initial *o*-xylene concentration per second, and n_N (mol) is the molar amount of the noble metal (Au and Pd)). The *o*-xylene oxidation rates can be calculated according to the activity data and amounts of Au and Pd in the supported Au–Pd– x M samples, and the results are summarized in Table 2. The TOF_N (357.2 μ s) and *o*-xylene reaction rate at 140 °C (2.59 μ mol/(g_N s)) over Au–Pd–0.22Fe/3DOM Mn_2O_3 were twice as much as those (129.1 μ s and 0.93 μ mol/(g_N s),

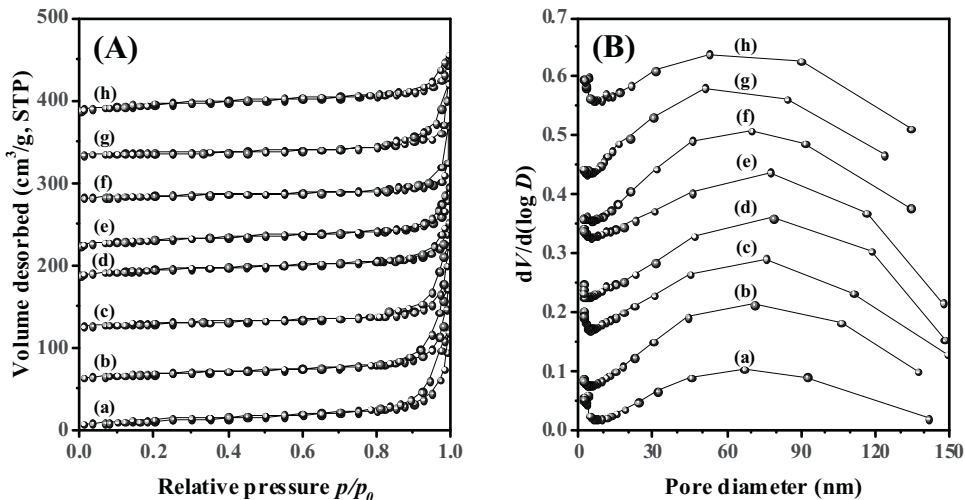


Fig. 3. (A) Nitrogen adsorption–desorption isotherms and (B) pore-size distributions of (a) Au–Pd–0.13Mn/3DOM Mn₂O₃, (b) Au–Pd–0.21Mn/3DOM Mn₂O₃, (c) Au–Pd–0.47Mn/3DOM Mn₂O₃, (d) Au–Pd–1.96Mn/3DOM Mn₂O₃, (e) Au–Pd–0.19Cr/3DOM Mn₂O₃, (f) Au–Pd–0.22Fe/3DOM Mn₂O₃, (g) Au–Pd–0.21Co/3DOM Mn₂O₃, and (h) Au–Pd/3DOM Mn₂O₃.

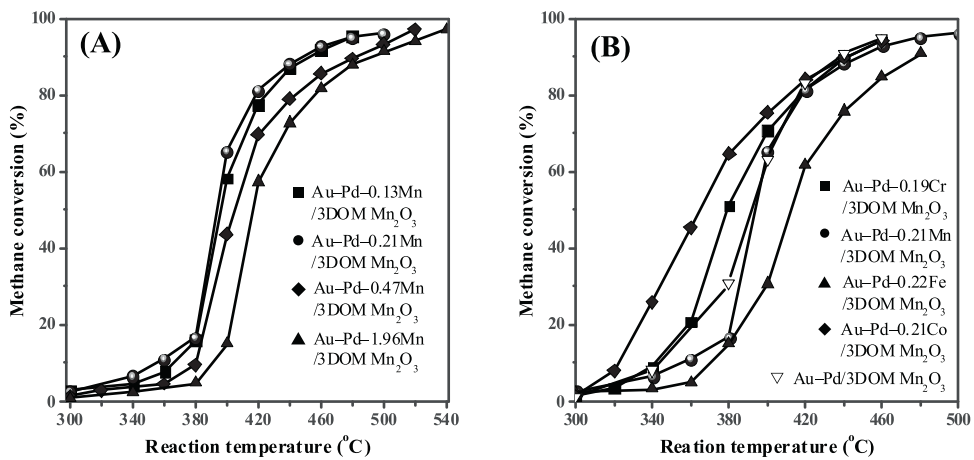


Fig. 4. Methane conversion as a function of reaction temperature over (A) Au–Pd–xMn/3DOM Mn₂O₃ ($x = 0.13\text{--}1.96$) and (B) Au–Pd–xM/3DOM Mn₂O₃ ($x = 0.19\text{--}0.22$; M = Mn, Cr, Fe, and Co) at SV = 40,000 mL/(g h).

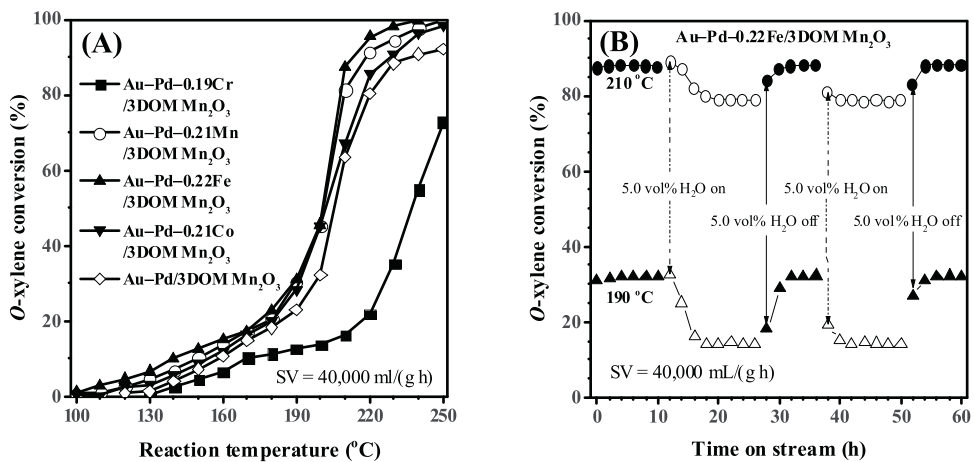


Fig. 5. (A) O-xylene conversion versus reaction temperature over Au–Pd–xM/3DOM Mn₂O₃ (M = Mn, Cr, Fe, and Co) and (B) o-xylene conversion as a function of on-stream reaction time in the presence or absence of 5.0 vol% water vapor at different temperatures over Au–Pd–0.22Fe/3DOM Mn₂O₃.

respectively) over Au–Pd/3DOM Mn₂O₃. This result suggests that doping a transition metal into Au–Pd NPs could greatly enhance the catalytic activity of the supported Au–Pd for o-xylene

oxidation. In other words, oxygen activation ability might be an important factor in enhancing the catalytic performance of the transition metal-doped samples. We believe that the strategy of

Table 2
Catalytic activities and apparent kinetic parameters of the samples for *o*-xylene oxidation at SV = 40,000 mL/(gh).

Sample	o-xylene oxidation			Oxidation at 140 °C			Kinetic parameter		
	T _{10%} (°C)	T _{50%} (°C)	T _{90%} (°C)	o-xylene conversion (%)	TOF _N ($\times 10^{-6} \text{ s}^{-1}$)	Reaction rate ($\times 10^{-6} \text{ mol}/(\text{g}_N \text{ s})$)	A (s^{-1})	E _a (kJ/mol)	R ²
Au-Pd/3DOM Mn ₂ O ₃	158	206	240	4.0	129.1	0.93	51.7 × 10 ⁶	71.7	0.9908
Au-Pd-0.19Cr/3DOM Mn ₂ O ₃	167	218	—	2.4	83.5	0.60	142.1 × 10 ⁶	77.1	0.9917
Au-Pd-0.21Mn/3DOM Mn ₂ O ₃	148	203	221	6.8	241.8	1.75	13.5 × 10 ⁶	65.3	0.9970
Au-Pd-0.22Fe/3DOM Mn ₂ O ₃	140	202	213	10.0	357.2	2.59	2.5 × 10 ⁶	58.2	0.9987
Au-Pd-0.21Cr/3DOM Mn ₂ O ₃	154	204	229	5.8	207.1	1.49	33.7 × 10 ⁶	69.3	0.9864

doping transition metal into noble metal NPs might be efficient for enhancing the catalytic activity of the supported noble metal catalysts.

The *o*-xylene reaction rate (2.59 μmol/(g_N s)) over Au-Pd-0.22Fe/3DOM Mn₂O₃ was much higher than that (1.72 μmol/(g_N s)) over 3.7 wt% Au/Co₃O₄ [36]. The sequence of TOF_N or *o*-xylene reaction rate at 140 °C of each sample was highly related with its catalytic performance. We tentatively use the T_{90%} to make a comparison on catalytic performance of the samples for *o*-xylene oxidation. The T_{90%} of 213 °C over Au-Pd-0.22Fe/3DOM Mn₂O₃ (1000 ppm *o*-xylene at SV = 40,000 mL/(g h)) was much lower than that (ca. 330 °C) over 4.4 wt% H₂SO₄ Pt/AC (1000 ppm *o*-xylene at SV = 8000 h⁻¹) [37], that (ca. 250 °C) over 1.0 wt% Pd/Co₃O₄ (3DL) (150 ppm *o*-xylene at SV = 60,000 mL/(g h)) [38], but similar to that (ca. 203 °C) over 1.0 wt% Pd/Co₃O₄ (3D) (150 ppm *o*-xylene at SV = 60,000 mL/(g h)) [4] and that (ca. 222 °C) over 0.30 wt% Pt/HBEA (50) (1700 ppm *o*-xylene at SV = 36,857 mL/(g h)) [39]. Therefore, our Au-Pd-0.22Fe/3DOM Mn₂O₃ catalyst performed well, as compared with the catalysts reported in the literature.

It is well known that catalytic activity for the oxidation of VOCs was negatively affected by water vapor introduced to the feed stream. Therefore, examination of water vapor effect on activity is meaningful. We carried out the experiment of introducing 5.0 vol% water vapor to the reaction system at 210 or 190 °C and SV = 40,000 mL/(g h) over the Au-Pd-0.22Fe/3DOM Mn₂O₃ sample for *o*-xylene oxidation, and the results are shown in Fig. 5B. It is observed that the *o*-xylene conversion dropped by ca. 10% at 210 °C or ca. 18% at 190 °C when 5.0 vol% water vapor was introduced, and the conversion could be gradually restored to its original value when the water vapor was cut off. After 60 h of on-stream reaction, there was no significant loss in catalytic activity, indicating that the Au-Pd-0.22Fe/3DOM Mn₂O₃ sample was catalytically stable for *o*-xylene oxidation under the adopted reaction conditions. For the Au-Pd-xM/3DOM Mn₂O₃ samples, there might be three main factors influencing their catalytic performance in the presence of water vapor. Due to the existence of Au clusters, O₂ could be conveniently activated by formation of hydroperoxyl species via the H-transfer reactions (O₂^{*} + H₂O^{*} → OOH^{*} + OH^{*} and OOH^{*} → O^{*} + OH^{*}) in the presence of water vapor [40]. As an active phase, PdO was easily changed to Pd(OH)₂ species through the reaction of PdO + H₂O → Pd(OH)₂ in the presence of water vapor, where the Pd(OH)₂ was ordinarily regarded as an inactive phase [41]. A competitive adsorption between H₂O and *o*-xylene as well as O₂ might also give rise to a decrease in catalytic performance for *o*-xylene oxidation. In one of our previous works, a positive effect was observed for toluene oxidation over the 1.99AuPd/3DOM Co₃O₄ catalyst in the presence of 1.0 vol% water vapor, but a decrease in activity occurred with the rise in water vapor concentration from 1.0 to 2.0 vol% [13]. We believe that the enhanced activation of oxygen by Au clusters resulted in activity enhancement in the presence of water vapor at low concentrations (< 1.0 vol%); when the water vapor concentration increased, however, the other two factors might dominate the influence on catalytic performance. Herein, the competitive adsorption between H₂O and *o*-xylene as well as O₂ and formation of Pd(OH)₂ were responsible for the drop in *o*-xylene conversion in the presence of 5.0 vol% water vapor. The significant loss in *o*-xylene conversion at a lower temperature over Au-Pd-0.22Fe/3DOM Mn₂O₃ was related to the more difficult desorption of adsorbed water molecules and decomposition of Pd(OH)₂, as compared to that at a higher temperature.

It is known that oxidation of VOCs obeys a reaction mechanism of first order toward VOC concentration and zero order toward O₂ concentration in the excessive amount of oxygen [25,36]. Hence, it is reasonably assumed that oxidation of *o*-xylene at an *o*-xylene/O₂ molar ratio of 1/200 would follow a first-order

reaction mechanism with respect to *o*-xylene concentration (*c*): $r = -kc = (-A\exp(-E_a/RT))c$, where *r* is the reaction rate (mol/s), *k* the rate constant (s^{-1}), *A* the pre-exponential factor (s^{-1}), and *E_a* the apparent activation energy (kJ/mol). The *k* values could be calculated from the reaction rates and reactant conversions at different SVs (e.g., 20,000, 40,000, and 80,000 mL/(g h)) and reaction temperatures. Fig. S4 shows the Arrhenius plots for *o*-xylene oxidation over Au-Pd-0.22Fe/3DOM Mn₂O₃ at different SVs (Fig. S4A) and Au-Pd-*xM*/3DOM Mn₂O₃ at a SV of 40,000 mL/(g h) (Fig. S4B), and their apparent activation energies are summarized in Table 2. The apparent activation energy (*E_a*) for *o*-xylene oxidation increased in the sequence of Au-Pd-0.22Fe/3DOM Mn₂O₃ (58.2 kJ/mol) < Au-Pd-0.21Mn/3DOM Mn₂O₃ (65.3 kJ/mol) < Au-Pd-0.21Co/3DOM Mn₂O₃ (69.3 kJ/mol) < Au-Pd/3DOM Mn₂O₃ (71.7 kJ/mol) < Au-Pd-0.19Cr/3DOM Mn₂O₃ (77.1 kJ/mol). This result suggests that *o*-xylene oxidation might take place easier over the Fe doped 3DOM Mn₂O₃-supported Au-Pd sample than the other transition metal-doped counterparts. The difference in *E_a* of the samples for *o*-xylene oxidation might be associated with the different modification effect of transition metals on the microstructure of the Au-Pd NPs [15].

3.3. Reducibility

Reducibility of a catalyst is highly related to its performance. Fig. 6 illustrates the H₂-TPR profiles of the Au-Pd-*xM*/3DOM Mn₂O₃ samples, and their quantitative analysis results are listed in Table S4. There were two main reduction steps for each of the samples. It is generally believed that *M* is thermally unstable after pretreated in an O₂ flow at 300 °C for 1 h, giving rise to a phase transfer from metallic *M* to MO_y. The reduction bands below 310 °C could be assigned to the reduction of Au^{δ+}, PdO_y, and MO_y species as well as the removal of adsorbed oxygen species [12], whereas the reduction bands above 310 °C could be ascribed to the reduction of Mn₂O₃. Specifically, the reduction band centered at 404 and 608 °C were due to the reduction of surface Mn³⁺ to Mn²⁺ and bulk Mn³⁺ to Mn²⁺ [21], respectively. It is understandable that the reduction of Au^{δ+} and PdO_y species together with adsorbed oxygen species was easier than that of MO_y, hence the two reduction peaks below 310 °C could be attributed to the reduction of Au^{δ+} and PdO_y together with adsorbed oxygen species (the 1st peak) and the reduction of MO_y (the 2nd peak), respectively. Obviously, the second reduction peak shifted to a higher temperature (from 170 to 240 °C) with the rise in Mn amount (*x*) doped to Au-Pd-*xMn* from 0.13 to 0.47, a result possibly due to the enhanced strong interaction between Au-Pd-Mn NPs and 3DOM Mn₂O₃, especially between the MnO_y and 3DOM Mn₂O₃ support. The second reduction peak disappeared and the first reduction peak shifted to 150 °C for the Au-Pd-1.96Mn/3DOM Mn₂O₃ sample. Due to a high Mn content in the Au-Pd-1.96Mn NPs, the first reduction peak of this sample shifted to a higher temperature. Among the Au-Pd-*xM*/3DOM Mn₂O₃ (*M*=Mn, Cr, Fe, and Co) samples, Au-Pd-0.22Fe/3DOM Mn₂O₃ possessed the best low-temperature reducibility: the lowest reduction peaks (130 and 150 °C) and a high H₂ consumption rate (21.2 mmol/(g_{cat} s)) at 130 °C. The H₂ consumption of the Au-Pd-*xM*/3DOM Mn₂O₃ samples below 310 °C and between 310 and 700 °C was in the ranges of 2.41–3.98 and 0.21–0.98 mmol/g_{cat} (Table S4), respectively.

3.4. Surface elemental composition, metal oxidation state, and oxygen species

XPS is an efficient technique to determine the surface element compositions and surface species of a catalyst. Figs. S5–S8 illustrate the Mn 2p_{3/2}, Au 4f, Pd 3d, and O 1s XPS spectra of the samples,

and the surface element compositions are summarized in Table 3. It is observed from Fig. S5 that each of the Mn 2p_{3/2} spectra was asymmetrical and could be decomposed into three components: surface Mn²⁺ species at binding energy (BE)=640.6 eV, surface Mn³⁺ species at BE=642.1 eV, and the satellite at BE=644.3 eV [6]. After doping of Mn to the Au-Pd/3DOM Mn₂O₃, the surface Mn³⁺/Mn²⁺ molar ratio slightly decreased from 1.37 to 1.02–1.26 (Table 3), indicating that the surface Mn²⁺ concentration increased. Such a decrease in Mn³⁺/Mn²⁺ molar ratio was due to the enhanced strong interaction between noble metal NPs and support, which was in good agreement with the results of H₂-TPR investigations. Due to the unique property of doped *M*, the interaction between the noble metal NPs and the support was different. The Co-doped Au-Pd/3DOM Mn₂O₃ sample possessed the lowest Mn³⁺/Mn²⁺ molar ratio (1.17), suggesting that there was the strongest interaction between the Au-Pd-Co and 3DOM Mn₂O₃.

Using the curve-fitting approach, the Au 4f spectrum of each sample could be decomposed into two sets of components (Fig. S6): the ones at BE=83.3 and 87.4 eV were due to the surface Au⁰ species, whereas the ones at BE=85.0 and 89.0 eV were due to the surface Au^{δ+} species [5,22]. The Au^{δ+}/Au⁰ molar ratios of the samples were in the range of 0.29–0.38. It has been reported that a higher Au^{δ+}/Au⁰ molar ratio was an indication of a better ability in activating oxygen molecules [24,25], thus enhancing the oxidation of VOCs. Fig. S7 shows the Pd 3d spectra of the samples, and each Pd 3d spectrum could also be decomposed into four components: the ones at BE=335.3 and 340.4 eV were assignable to the surface Pd⁰ species, whereas the ones at BE=337.3 and 342.4 eV were attributable to the surface Pd²⁺ species [42,43]. The Pd²⁺/Pd⁰ molar ratios (0.46–1.33) of the *M*-doped Au-Pd/3DOM Mn₂O₃ samples were lower than that (1.83) of the Au-Pd/3DOM Mn₂O₃ sample. A modification on the Au-Pd structure by doped *M* could lead to the change of Pd or Au species. Due to the unique ability to activate methane, Pd²⁺ species was highly active for methane oxidation. Furthermore, Au^{δ+} and Pd²⁺ species could also facilitate activate oxygen, therefore showing good performance for methane or VOCs oxidation [31,43].

Generally speaking, the ability to activate oxygen correlates with the activity of a catalyst for organics oxidation. One can decompose the asymmetrical O 1s spectrum (Fig. S8) of each sample into three components: the surface lattice oxygen (O_{latt}) species at BE=529.4 eV, the surface adsorbed oxygen (O_{ads}, e.g., O₂[−], O₂^{2−}, O[−], OH[−] or CO₃^{2−}) species at BE=531.3–531.4 eV, and the surface adsorbed molecular water at BE=533.3–533.4 eV [13,44]. Since the sample was pretreated at 450 °C in an O₂ flow before XPS measurement, the surface hydroxyl and carbonate species would be minimized. In other words, the O_{ads} species were mainly O₂[−], O₂^{2−} or O[−] species. Such oxygen species were active for the oxidation of hydrocarbons at low temperatures [44]. As summarized in Table 3, the surface O_{ads}/O_{latt} molar ratio on Au-Pd-*xMn*/3DOM Mn₂O₃ decreased in the order of Au-Pd-0.13Mn/3DOM Mn₂O₃ (1.25)>Au-Pd-0.21Mn/3DOM Mn₂O₃ (0.98)>Au-Pd/3DOM Mn₂O₃ (0.85)≈Au-Pd-0.47Mn/3DOM Mn₂O₃ (0.84)>Au-Pd-1.96Mn/3DOM Mn₂O₃ (0.48). With the doping of Mn, the O_{ads}/O_{latt} molar ratio of the sample first increased and then dropped with the decrease in amounts of Au and Pd. This result suggests that Au and Pd could play an important role in activating O₂ molecules, and doping a certain amount of *M* could enhance the ability to activate oxygen molecules. For the different metal-doped samples, the O_{ads}/O_{latt} molar ratio decreased in the sequence of Au-Pd-0.19Fe/3DOM Mn₂O₃ (1.18)>Au-Pd-0.21Mn/3DOM Mn₂O₃ (0.98)>Au-Pd-0.21Co/3DOM Mn₂O₃ (0.91)>Au-Pd-0.22Cr/3DOM Mn₂O₃ (0.71).

In order to evaluate the mobility of lattice oxygen, O₂-TPD experiments of the samples were carried out, and their profiles are shown in Fig. 7. Considering that the water species on the

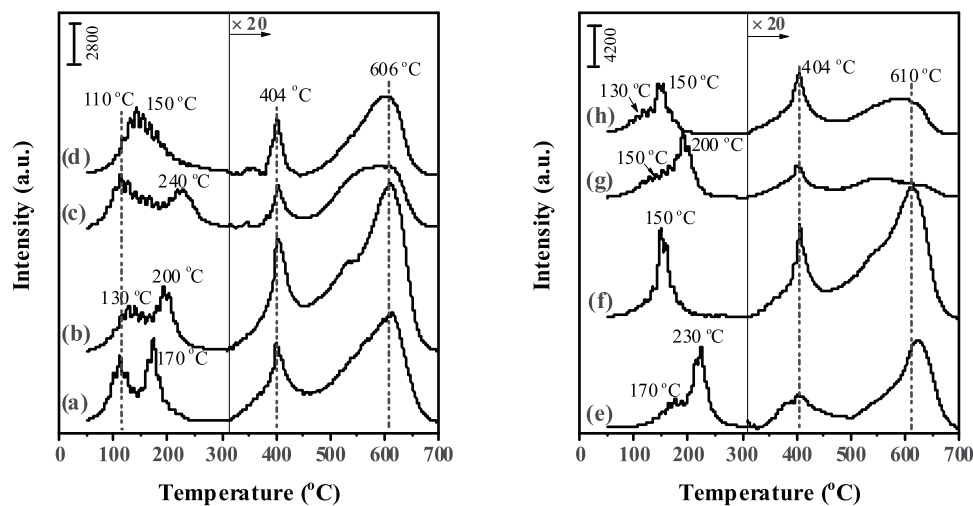


Fig. 6. H_2 -TPR profiles of (a) Au-Pd-0.13Mn/3DOM Mn_2O_3 , (b) Au-Pd-0.21Mn/3DOM Mn_2O_3 , (c) Au-Pd 0.47Mn/3DOM Mn_2O_3 , (d) Au-Pd-1.96Mn/3DOM Mn_2O_3 , (e) Au-Pd-0.19Cr/3DOM Mn_2O_3 , (f) Au-Pd-0.22Fe/3DOM Mn_2O_3 , (g) Au-Pd-0.21Co/3DOM Mn_2O_3 , and (h) Au-Pd/3DOM Mn_2O_3 .

Table 3
Surface element compositions, surface Pd^{2+} contents, and oxygen desorption of the Au-Pd- $xM/3\text{DOM Mn}_2\text{O}_3$ samples.

Sample	Surface element composition				Surface Pd^{2+} content (wt%)	Oxygen desorption (mmol/g _{cat})			
	$\text{Mn}^{3+}/\text{Mn}^{2+}$ molar ratio	$\text{Au}^{\delta+}/\text{Au}^0$ molar ratio	$\text{Pd}^{2+}/\text{Pd}^0$ molar ratio	$\text{O}_{\text{ads}}/\text{O}_{\text{latt}}$ molar ratio		<250 °C (1st peak)		250–470 °C (2nd peak)	
						<250 °C (1st peak)	250–470 °C (2nd peak)	470–570 °C	
Au-Pd/3DOM Mn_2O_3	1.37	0.36	1.83	0.85	0.634	1.31	9.66	5.86	
Au-Pd-0.13Mn/3DOM Mn_2O_3	1.26	0.35	0.54	1.25	0.326	1.58	28.83	24.81	
Au-Pd-0.21Mn/3DOM Mn_2O_3	1.23	0.33	0.58	0.98	0.327	1.41	21.77	13.24	
Au-Pd-0.47Mn/3DOM Mn_2O_3	1.17	0.30	0.46	0.84	0.246	0.88	13.47	7.38	
Au-Pd-1.96Mn/3DOM Mn_2O_3	1.02	0.29	0.53	0.48	0.163	0.75	14.61	9.83	
Au-Pd-0.19Cr/3DOM Mn_2O_3	1.25	0.32	0.80	0.71	0.396	1.04	11.20	10.00	
Au-Pd-0.22Fe/3DOM Mn_2O_3	1.29	0.38	0.53	1.18	0.305	1.57	20.74	13.96	
Au-Pd-0.21Co/3DOM Mn_2O_3	1.17	0.37	1.33	0.91	0.497	1.34	4.32	3.68	

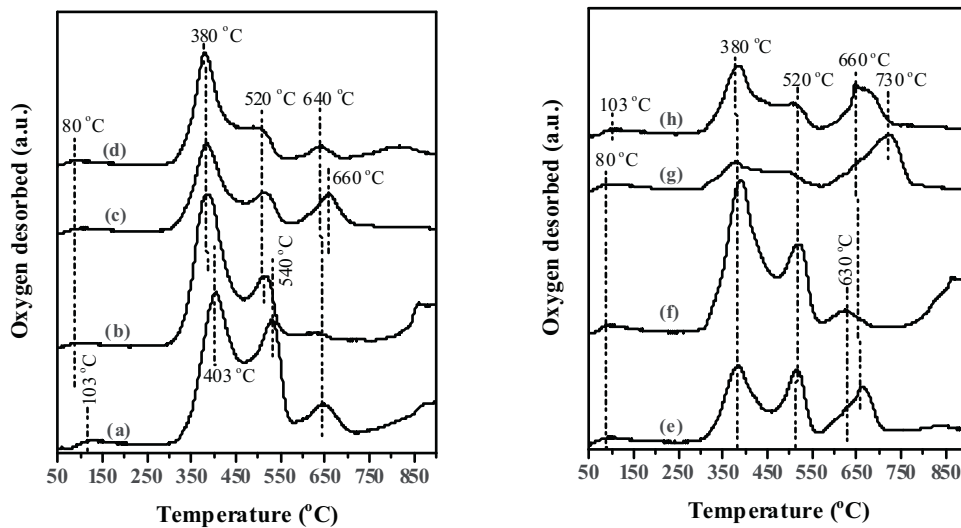


Fig. 7. O_2 -TPD profiles of (a) Au-Pd-0.13Mn/3DOM Mn_2O_3 , (b) Au-Pd-0.21Mn/3DOM Mn_2O_3 , (c) Au-Pd-0.47Mn/3DOM Mn_2O_3 , (d) Au-Pd-1.96Mn/3DOM Mn_2O_3 , (e) Au-Pd-0.19Cr/3DOM Mn_2O_3 , (f) Au-Pd-0.22Fe/3DOM Mn_2O_3 , (g) Au-Pd-0.21Co/3DOM Mn_2O_3 , and (h) Au-Pd/3DOM Mn_2O_3 .

samples were removed after such pretreatments, the weak signal at low temperatures (<250 °C) was due to the desorption of surface chemisorbed oxygen (O_2^- , O_2^{2-} or O^-) species; the main peak centered at 380 or 403 °C and the shoulder at 520 or 540 °C was attributable to the desorption of the structural oxygen species from PdO and/or MO_y ; and the peaks above 570 °C were assignable

to the desorption of the lattice oxygen species from Mn_2O_3 [12,44]. The doping of M enhanced the adsorbed oxygen species amount of the sample, and the 1st oxygen desorption peak shifted to a lower temperature (from 103 to 80 °C). This result indicates that the doping of M improved the oxygen activation ability of the 3DOM Mn_2O_3 -supported Au-Pd sample. After estimating

the oxygen desorption, one can realize that similar to the XPS results, with the rise in Mn doped amount, the desorption of the 1st peak from the sample first increased and then decreased, suggesting that Au and Pd were the key species for the activation of O₂ molecules and doping a certain amount of M could enhance the O₂ activation ability of the sample. For the different metal-doped samples, the desorption of the 1st peak from the sample decreased in the order of supported Au–Pd–0.19Fe/3DOM Mn₂O₃ (1.57 mmol/g) > Au–Pd–0.21Mn/3DOM Mn₂O₃ (1.41 mmol/g) > Au–Pd–0.21Co/3DOM Mn₂O₃ (1.34 mmol/g) > Au–Pd (1.31 mmol/g) > Au–Pd–0.22Cr/3DOM Mn₂O₃ (1.04 mmol/g).

4. Discussion

Over the Pd-based catalysts, the oxidation of an organic obeys the Mars–van Krevelen (MVK) mechanism, in which the reaction takes place via a redox cycle of the catalyst surface. Methane or oxylene could react with the chemisorbed oxygen to yield the total oxidation products. Therefore, a catalyst with good oxygen activation ability would be active for the oxidation of organics. According to the Langmuir–Hinshelwood (LH) model, the oxidation of an organic takes place via the reaction of the adsorbed oxygen and adsorbed organic species on the catalyst surface, involving a rate-limiting step. The MVK and LH models have successfully explained the oxidation of a number of organics [45–47].

It is generally known that PdO was the active site for methane oxidation over the Pd-based catalysts, and the concentration of surface PdO species was an important factor influencing methane oxidation. The Pd 3d XPS results reveal that doping M to the Au–Pd/3DOM Mn₂O₃ sample caused a decrease in Pd²⁺/Pd⁰ molar ratio, but an enhancement in catalytic activity was observed for methane oxidation. For the Au–Pd–xMn/3DOM Mn₂O₃ samples, the rise in Mn doped amount led to the drop in total Pd content, i.e., the decrease in active site amount. In order to figure out the relationship of Pd species with methane oxidation activity over the Au–Pd–xM/3DOM Mn₂O₃ samples, it is necessary to estimate the surface Pd²⁺ amount on each sample. Considering that the particle sizes of Au–Pd–xM in the samples were rather close, we calculate the surface Pd²⁺ content of each sample using the formula of (Pd²⁺/(Pd²⁺ + Pd⁰) molar ratio) × (Pd content (wt%) in each sample), as summarized in Table 3. Fig. 8 illustrates the T_{10%} and T_{50%} for methane oxidation as a function of surface Pd²⁺ content on the Au–Pd–xM/3DOM Mn₂O₃ samples. One can clearly see a good relationship between surface Pd²⁺ content and catalytic activity over these samples: the activity of the sample increased with the rise in surface Pd²⁺ content. Among the Au–Pd–xM/3DOM Mn₂O₃ samples, Au–Pd–0.21Co/3DOM Mn₂O₃ performed the best, although Au–Pd–0.22Fe/3DOM Mn₂O₃ possessed the highest concentration of adsorbed oxygen. If only surface oxygen participates in the oxidation of methane (i.e., obeying the MVK mechanism), the Au–Pd–0.22Fe/3DOM Mn₂O₃ sample would perform the best. It should be noted that unlike the Au–Pd–xM/3DOM Mn₂O₃ samples, the Au–Pd/3DOM Mn₂O₃ sample exhibited a higher surface Pd²⁺ content but a lower activity for methane oxidation. It is well known that alloying a metal with Pd can modify the electronic state of Pd particles, thus influencing its catalytic performance for methane oxidation [32]. The results demonstrate that the amount of exposed Pd²⁺ species could influence the methane oxidation activity of the samples with a similar alloy structure. Since doping a similar amount of a different transition metal could change the structure of Au–Pd NPs, the induced effect on catalytic performance was dependent not only on the chemisorbed oxygen species activated by the exposed Pd²⁺ species, but also on the adsorption ability of methane molecules. Changing the volumetric ratio of oxygen to

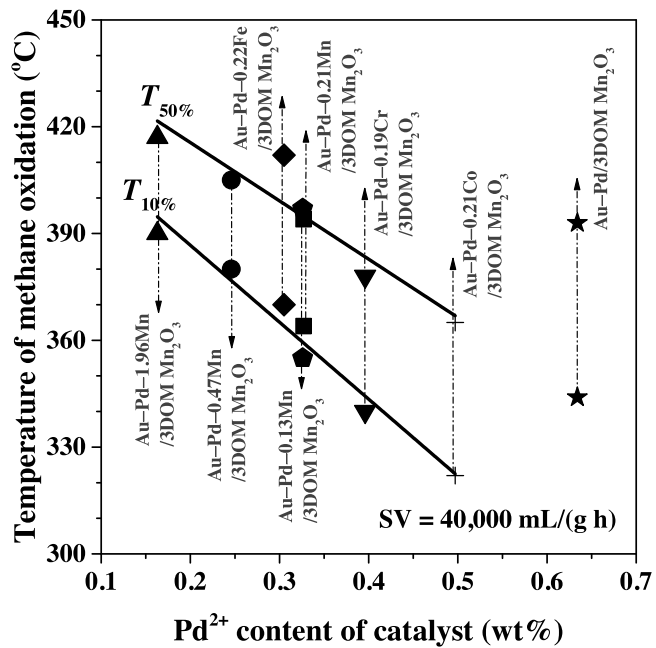


Fig. 8. T_{10%} and T_{50%} for methane oxidation as a function of surface Pd²⁺ content of the Au–Pd–xM/3DOM Mn₂O₃ samples.

methane is a good option to detect its effect on enhancement in oxygen activation or methane adsorption after doping of the transition metals. For example, Ortloff and coworkers [48] evaluated oxygen conversions at different partial pressures of methane, and observed that oxygen conversion increased with the rise in methane partial pressure. Such a result indicates that adsorption of methane or the subsequent dissociation of methane was predominantly assumed to limit the overall reaction rate under oxygen extra conditions over the supported Pt catalyst. In the present work, we obtained the information related to the oxygen activation ability using the XPS and O₂-TPD techniques and the methane adsorption ability of the samples using the CH₄-TPD technique. One can realize that the doping of transition metals enhanced the methane adsorption ability of the noble metal alloys, thus improving the catalytic performance of the samples. That is to say, the good catalytic performance of the Co-doped sample could be attributed to the enhanced methane activation ability as well as better methane adsorption ability. The results were in good agreement with those reported by Ortloff et al. [48].

That is to say, unlike the conventional Pd-based catalysts over which the MVK mechanism governs the oxidation of methane, the transition metal-doped Au–Pd/3DOM Mn₂O₃ samples preferred to obey the LH mechanism [49]. One of our previous works demonstrated that doping Co to Pd/3DOM CeO₂ could improve the ability of methane adsorption, hence beneficial for methane activation and its deep oxidation [33]. Based on the results reported in the literature and those obtained in the present work, we conclude that (i) the activation of methane by the exposed Pd²⁺ species was the rate-limiting step in the oxidation of methane; (ii) doping an appropriate amount of the transition metal could modify the structure of Au–Pd NPs, thus improving the adsorption and activation ability of reactant molecules and hence enhancing the catalytic performance of the sample for methane oxidation. In other words, good methane activation ability together with better methane adsorption ability responding to the good catalytic performance over the Co doped sample.

It has been reported that the MVK model was suitable for the catalytic oxidation of VOCs over metal oxide or supported Pd catalysts under an oxygen-rich condition [47,50]. This model involves in two

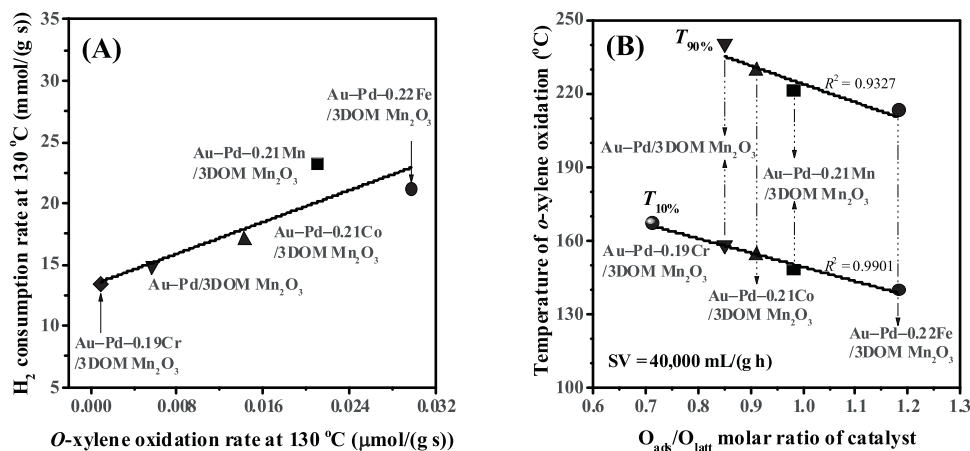


Fig. 9. (A) H₂ consumption rate versus o-xylene oxidation rate at the temperature of 140 °C and (B) T_{10%} and T_{90%} for o-xylene oxidation as a function of O_{ads}/O_{latt} molar ratio over the Au-Pd-xM/3DOM Mn₂O₃ samples.

redox steps: VOCs are first oxidized by the adsorbed oxygen species on the catalyst surface, and the gas-phase oxygen molecules were then activated by the catalyst. The oxygen on the catalyst surface could be either the chemisorbed or the lattice oxygen depending on the reaction temperature. At a relatively low temperature, the chemisorbed oxygen species are the main oxygen species that react with VOCs. Therefore, enhancing the oxygen activation ability of a catalyst can play a positive role on VOCs oxidation. Fig. 9A shows the H₂ consumption rate versus o-xylene oxidation rate at 130 °C over the Au-Pd-0.20M/3DOM Mn₂O₃ samples. Apparently, the catalytic activity was intimately related to the H₂ consumption rate, suggesting that catalytic performance was associated with the low-temperature reducibility. It is generally believed that the low-temperature reducibility of a sample is related to its adsorbed oxygen species since the chemisorbed oxygen species are more readily reduced by hydrogen at low temperatures.

The reduction of oxidized noble metal species also occurs at low temperatures for the supported noble metal samples. Oxidized noble metal species (e.g., Au^{δ+} and PdO_y) are beneficial for oxygen activation. Hence, we think that a higher concentration of adsorbed oxygen species (i.e., better activation ability of adsorbed oxygen species) could be related to better low-temperature reducibility. In the present work, the first reduction peak was assigned to the reduction of adsorbed oxygen and/or Au^{δ+} and PdO_y species. It is concluded that the higher concentration of adsorbed oxygen species might be accountable for the better catalytic performance of the Au-Pd-0.22Fe/3DOM Mn₂O₃ and Au-Pd-0.21Mn/3DOM Mn₂O₃ samples. In other words, good catalytic activity of the samples for o-xylene oxidation might be due to their good ability to activate oxygen molecules [13,36].

In order to confirm the relationship between adsorbed oxygen species and catalytic activity, the T_{10%} and T_{90%} for o-xylene oxidation as a function of O_{ads}/O_{latt} molar ratio over the Au-Pd-xM/3DOM Mn₂O₃ samples are presented in Fig. 9B. It is obviously seen that the T_{10%} or T_{90%} decreased with the rise in O_{ads}/O_{latt} molar ratio. Among these samples, Au-Pd-0.22Fe/3DOM Mn₂O₃ possessed the highest O_{ads}/O_{latt} molar ratio and the T_{10%} or T_{90%} was the lowest. According to the results of O 1s XPS and O₂-TPD investigations, the O_{ads}/O_{latt} molar ratio on each sample reflected its chemisorbed oxygen concentration, i.e., the oxygen activation ability. Au and Pd were the key components in activating O₂ molecules, and doping a certain amount of M could enhance the oxygen activation ability. Based on the above results, we conclude that doping a certain amount of the transition metal to Au-Pd/3DOM Mn₂O₃ could modify the microstructure of the Au-Pd alloy NPs, thus improving the oxygen activation ability. Among all

of the samples, Au-Pd-0.22Fe/3DOM Mn₂O₃ exhibited the highest catalytic activity, which was associated with its enhanced activation of oxygen.

The studies on the kinetics of catalytic oxidation of alkanes (methane, ethane, propane, n-butane, and isobutene) over nickel, palladium, and platinum foils under an excessive oxygen condition indicates that the catalytic oxidation reactivity trend correlated with the strength of the C-H bond, that is to say, higher rates were observed for the longer and more branched hydrocarbon chains [51,52]. The difference in reaction rate observed for different hydrocarbons suggests that activation of the first C-H bond in saturated hydrocarbons might be the rate-limiting step during the oxidation process. In the present study, the activity of the sample increased with the rise in surface Pd²⁺ content on the transition metal-doped samples. This result indicates that activation of methane by the exposed Pd²⁺ species was the rate-limiting step in the oxidation of methane. Unlike the Au-Pd-xM/3DOM Mn₂O₃ samples, however, the Au-Pd/3DOM Mn₂O₃ sample exhibited a higher surface Pd²⁺ content but a lower catalytic activity for methane oxidation. In other words, there might be the other factors accountable for the lower performance of Au-Pd/3DOM Mn₂O₃. It has been also reported that methane possesses the greatest C-H bond strength (the gas phase dissociation enthalpy of the H-CH₃ bond = 104 kcal/mol) among all of the saturated hydrocarbons [53]. The activation energy of methane dissociative adsorption on certain surfaces of some transition metals was lower (6–10 kcal/mol) [54], indicating that some transition metals might be beneficial for methane adsorption. Such a deduction was in good agreement with our previously reported result that Co species could significantly enhance the ability of methane adsorption on the CeO₂-supported Pd catalysts [33]. Frennet et al. have investigated the adsorption of methane on polycrystalline metals, and concluded that not only the height of the barrier (activation energy), but also the geometrical configuration of the transition complex were the crucial factor of influencing the catalytic activity of the sample [55]. The doping of a transition metal could modify the microstructure of Au-Pd NPs, thus increasing the probability of methane adsorption on the supported alloy catalyst. In our study, the doping of the transition metal into Au-Pd NPs possibly enhanced the methane adsorption ability of the supported Au-Pd samples. Hence, methane oxidation on the transition metal-doped Au-Pd/3DOM Mn₂O₃ samples might obey the Langmuir-Hinshelwood mechanism. Considering that higher rates were observed for the oxidation of longer and more branched hydrocarbons reported above, the catalytic activation of the C-H bond in o-xylene would be much easier, as compared with the difficulty in methane activation. Taking into account the good

relationship between surface adsorbed oxygen species concentration and catalytic performance, we believe that the rate-determining step of *o*-xylene oxidation would be the activation of oxygen molecules. That might be the reason why there was a difference in catalytic performance for methane and *o*-xylene oxidation over the Au–Pd–0.21Co/3DOM Mn₂O₃ and Au–Pd–0.22Fe/3DOM Mn₂O₃ samples.

5. Conclusions

The Au–Pd–*xM*/3DOM Mn₂O₃ (*M*=Mn, Cr, Fe, and Co) samples with a metal loading of 1.86–1.97 wt% were prepared using the modified PVA-protected reduction and the gas bubble-assisted adsorption strategies. The Au–Pd–*xM* NPs with an average Au–Pd–*xM* particle size of 3.6–4.4 nm were highly dispersed on the wall surface of 3DOM Mn₂O₃. The Au–Pd–*xM*/3DOM Mn₂O₃ samples exhibited high catalytic activities for methane and *o*-xylene oxidation. Among the samples, Au–Pd–0.21Co/3DOM Mn₂O₃ showed the highest performance for methane oxidation (*T*_{10%}=322 °C and *T*_{50%}=365 °C), which was due to its highest surface Pd²⁺ content and enhanced methane adsorption ability; however, Au–Pd–0.22Fe/3DOM Mn₂O₃ performed the best for *o*-xylene oxidation (*T*_{10%}=140 °C and *T*_{90%}=213 °C), which was related to its highest amount of adsorbed oxygen species. It is concluded that doping an appropriate amount of the transition metal to Au–Pd/3DOM Mn₂O₃ could modify the microstructure of the Au–Pd NPs, thus improving the oxygen activation and adsorption methane ability. We believe that such a strategy of modifying noble metal catalysts would be meaningful in enhancing catalytic efficiency of organics oxidation.

Acknowledgements

This work was supported by the NSF of China (21377008, 21477005, and 21677004), National High Technology Research and Development Program of China (863 Program, 2015AA034603), Beijing Nova Program (Z141109001814106), the NSF of Beijing Municipal Commission of Education (KM201410005008), Foundation on the Creative Research Team Construction Promotion Project of Beijing Municipal Institutions, and Scientific Research Base Construction–Science and Technology Creation Platform–National Materials Research Base Construction.

Appendix A. Supplementary data

Supplementary data associated with this article can be found, in the online version, at <http://dx.doi.org/10.1016/j.apcatb.2017.01.030>.

References

- [1] P.O. Larsson, A. Anderson, J. Catal. 179 (1998) 72–89.
- [2] S.C. Kim, W.G. Shim, Appl. Catal. B 98 (2010) 180–185.
- [3] H.X. Dai, Sci. Bull. 60 (2015) 1708–1710.
- [4] Y.F. Wang, C.B. Zhang, F.D. Liu, H. He, Appl. Catal. B 142–143 (2013) 72–79.
- [5] A.K. Sinha, K. Suzuki, M. Takahara, H. Azuma, T. Nonaka, K. Fukumoto, Angew. Chem. Int. Ed. 46 (2007) 2891–2894.
- [6] J.G. Deng, S.N. He, S.H. Xie, H.G. Yang, Y.X. Liu, G.S. Guo, H.X. Dai, Environ. Sci. Technol. 49 (2015) 11089–11095.
- [7] S.H. Xie, H.X. Dai, J.G. Deng, Y.X. Liu, H.G. Yang, Y. Jiang, W. Tan, A.S. Ao, G.S. Guo, Nanoscale 5 (2013) 11207–11219.
- [8] J.K. Edwards, B.E. Solsona, P. Landon, A.F. Carley, A. Herzing, C.J. Kiely, G.J. Hutchings, J. Catal. 236 (2005) 69–79.
- [9] D.I. Enache, J.K. Edwards, P. Landon, B. Solsona, A.F. Carley, A.A. Herzing, M. Watanabe, C.J. Kiely, D.W. Knight, G.J. Hutchings, Science 311 (2009) 362–365.
- [10] L. Kesavan, R. Tiruvalam, M.H.A. Rahim, M.I. Saiman, D.I. Enache, R.L. Jenkins, N. Dimitratos, J.A.L. Sanchez, S.H. Taylor, D.W. Knight, C.J. Kiely, G.J. Hutchings, Science 331 (2006) 195–199.
- [11] M.H.A. Rahim, M.M. Forde, R.L. Jenkins, C. Hammond, Q. He, N. Dimitratos, J.A.L. Sanchez, A.F. Carley, S.H. Taylor, D.J. Wilcock, D.M. Murphy, C.J. Kiely, G.J. Hutchings, Angew. Chem. Int. Ed. 52 (2013) 1280–1284.
- [12] S.H. Xie, J.G. Deng, Y.X. Liu, Z.H. Zhang, H.G. Yang, Y. Jiang, H. Arandiyan, H.X. Dai, C.T. Au, Appl. Catal. A 507 (2015) 82–90.
- [13] S.H. Xie, J.G. Deng, S.M. Zang, H.G. Yang, G.S. Guo, H. Arandiyan, H.X. Dai, J. Catal. 322 (2015) 38–48.
- [14] Z.X. Wu, J.G. Deng, Y.X. Liu, S.H. Xie, Y. Jiang, X.T. Zhao, J. Yang, H. Arandiyan, G.S. Guo, H.X. Dai, J. Catal. 332 (2015) 13–24.
- [15] S.J. Freakley, Q. He, J.H. Harrhy, L. Lu, D.A. Crole, D.J. Morgan, E.N. Ntaijua, J.K. Edwards, A.F. Carley, A.Y. Borisevich, C.J. Kiely, G.J. Hutchings, Science 351 (2016) 965–968.
- [16] J.P. Stassi, P.D. Zgolcic, S.R. de Miguel, O.A. Scelza, J. Catal. 306 (2013) 11–29.
- [17] A. Dutta, J.Y. Ouyang, ACS Catal. 5 (2015) 1371–1380.
- [18] G.X. Chen, Y. Zhao, G. Fu, P.N. Duchesne, L. Gu, Y.P. Zheng, X.F. Weng, M.S. Chen, P. Zhang, C.W. Pao, J.F. Lee, N.F. Zheng, Science 344 (2014) 495–499.
- [19] D.H. Sun, V. Mazumder, O. Metin, S.H. Sun, ACS Catal. 2 (2012) 1290–1295.
- [20] Y.E. Wu, D.S. Wang, G. Zhou, R. Yu, C. Chen, Y.D. Li, J. Am. Chem. Soc. 136 (2014) 11594–11597.
- [21] F. Wang, H.X. Dai, J.G. Deng, G.M. Bai, K.M. Ji, Y.X. Liu, Environ. Sci. Technol. 46 (2012) 4034–4041.
- [22] S.H. Xie, H.X. Dai, J.G. Deng, H.G. Yang, W. Han, H. Arandiyan, G.S. Guo, J. Hazard. Mater. 279 (2014) 392–401.
- [23] J.G. Deng, S.N. He, S.H. Xie, H.G. Yang, Y.X. Liu, H.X. Dai, Chem. J. Chin. Univ. 35 (2014) 1119–1129 (in Chinese).
- [24] Y.C. Wei, J. Liu, Z. Zhao, A.J. Duan, G.Y. Jiang, J. Catal. 287 (2012) 13–29.
- [25] H. Arandiyan, H.X. Dai, K.M. Ji, H.Y. Sun, J.H. Li, ACS Catal. 5 (2015) 1781–1793.
- [26] Y. Liu, B.C. Liu, Q. Wang, C.Y. Li, W.T. Hu, Y.X. Liu, P. Jing, W.Z. Zhao, J. Zhang, J. Catal. 296 (2012) 65–76.
- [27] H.N. Li, L. Zhang, H.X. Dai, H. He, Inorg. Chem. 48 (2009) 4421–4434.
- [28] J.R. Paredes, E. Díaz, F.V. Díez, S. Ordóñez, Energy Fuels 23 (2009) 86–93.
- [29] F. Kapteijn, J.A. Moulijn, A. Tarfaoui, Stud. Surf. Sci. Catal. 123 (1999) 525–541.
- [30] J.H. Park, J.H. Cho, Y.J. Kim, E.S. Kim, H.S. Han, C.H. Shin, Appl. Catal. B 160–161 (2014) 135–143.
- [31] F.F. Muñoz, R.T. Baker, A.G. Leyva, R.O. Fuentes, Appl. Catal. B 136–137 (2013) 122–132.
- [32] A. Satsuma, T. Tojo, K. Okuda, Y. Yamamoto, S. Arai, J. Oyama, Catal. Today 242 (2015) 308–314.
- [33] S.H. Xie, Y.X. Liu, J.G. Deng, X.T. Zhao, J. Yang, K.F. Zhang, Z. Han, H.X. Dai, J. Catal. 342 (2016) 17–26.
- [34] C. Chen, Y.H. Yeh, M. Cargnello, C.B. Murray, P. Fornasiero, R.J. Gorte, ACS Catal. 4 (2014) 3902–3909.
- [35] B.H. Yue, R.R. Zhou, Y.J. Wang, X.M. Zheng, Appl. Surf. Sci. 252 (2006) 5820–5828.
- [36] Y.X. Liu, H.X. Dai, J.G. Deng, X.W. Li, Y. Wang, H. Arandiyan, S.H. Xie, H.G. Yang, G.S. Guo, J. Catal. 305 (2013) 146–153.
- [37] W.G. Shim, S.C. Kim, Appl. Surf. Sci. 256 (2010) 5566–5571.
- [38] Y.F. Wang, C.B. Zhang, Y.B. Yu, R.L. Yue, H. He, Catal. Today 242 (2015) 294–299.
- [39] J. Tsou, L. Pinard, P. Magnoux, J.L. Figueiredo, M. Guisnet, Appl. Catal. B 46 (2003) 371–379.
- [40] C.R. Chang, X.F. Yang, B. Long, J. Li, ACS Catal. 3 (2013) 1693–1699.
- [41] R.S. William, D.P. Lisa, J. Phys. Chem. C 116 (2012) 8571–8578.
- [42] K.R. Priolkar, P. Bera, P.R. Sarode, M.S. Hegde, S. Emura, R. Kumashiro, N.P. Lalla, Chem. Mater. 14 (2002) 2120–2128.
- [43] H. Gabasch, K. Hayek, B. Klo1tzer, W. Unterberger, E. Kleimenov, D. Teschner, S. Zafeiratos, M. Halvecker, A. Knop-Gericke, R. Schlolg, B. Aszalos-Kiss, D. Zemlyanov, J. Phys. Chem. C 111 (2007) 7957–7962.
- [44] M. Piumenti, D. Fino, N. Russo, Appl. Catal. B 163 (2015) 277–287.
- [45] D. Ciuparu, M. Lyubovsky, E. Altman, L.D. Pfefferle, A. Datye, Catal. Rev. 44 (2002) 593–649.
- [46] P. Hurtado, S. Ordóñez, H. Sastre, F.V. Díez, Appl. Catal. B 51 (2004) 229–238.
- [47] S. Ordóñez, L. Bello, H. Sastre, R. Rosal, F.V. Díez, Appl. Catal. B 38 (2002) 139–149.
- [48] F. Ortloff, J. Bohnau, F. Graf, T. Kolb, Appl. Catal. B 182 (2016) 375–384.
- [49] M. Valden, J. Pere, M. Hirsimaki, S. Suohonen, M. Pessa, Surf. Sci. 377–379 (1997) 605–609.
- [50] C. He, P. Li, J. Cheng, Z.P. Hao, Z.P. Xu, Water Air Soil Pollut. 209 (2010) 365–376.
- [51] M. Aryafar, F. Zaera, Catal. Lett. 48 (1997) 173–183.
- [52] T. Maillet, C. Solleau, J. Barbier, D. Duprez, Appl. Catal. B 14 (1997) 85–95.
- [53] D. Ciuparu, M.R. Lyubovsky, E. Altman, L.D. Pfefferle, A. Datye, Catal. Rev. 44 (2002) 593–649.
- [54] Y.N. Wang, R.G. Herman, K. Klier, Surf. Sci. 279 (1992) 33–48.
- [55] A. Frennet, Catal. Rev. 10 (1974) 37–68.